AC Component-Based Control and Phase Shift Applications on Bidirectional Chopper With Auxiliary Full-Bridge Converter

Ghiffari Aby Malik Nasution, *Graduate Student Member, IEEE*, and Makoto Hagiwara, *Senior Member, IEEE*

***Abstract*—This article proposes the supplementary application of ac component-based control to a bidirectional chopper with an auxiliary converter when the dc current flowing in the chopper is zero. The proposed chopper is composed of a bidirectional chopper as the main converter, an auxiliary converter with a single full-bridge converter, and an inductor, where phase shift is additionally applied to the carrier wave of the auxiliary converter. This setup is theoretically able to reduce the switching-ripple current to 1/4 of that the conventional bidirectional chopper, which consequently allows smaller inductor to be used in the chopper. Furthermore, experimental results using a 2 kW down-scaled model further verify the theoretical analysis results on the switching-ripple current, and the validity of the ac component-based control based on the steady- and transient-state performances of the proposed chopper, along with its coordination with the conventional dc component-based control. Finally, theoretical comparison with the conventional bidirectional chopper, three-level flying capacitor converter, and a bidirectional chopper with an auxiliary converter with no phase shift is done with respect to the inductor volume, power loss, and efficiency to verify the benefits of phase shift application in the proposed chopper.**

***Index Terms*—AC component-based control, battery energy storage systems, nonisolated DC–DC converters, phase shift.**

I. Introduction

RECENTLY, battery energy storage system (BESS) utilization in electric railways has been gaining momentum due to its ability to recover the regenerative-braking energy, allow renewable applications, shave peak power during acceleration, and enable catenary-free operation [1], [2], [3], [4]. A conventional bidirectional chopper (CBC) is traditionally used to convert the voltage between the power source and the battery with the typical voltage from 600 V to 3 kV [5], [6], [7]. When BESS is used, it is imperative to reduce the mass and volume of the chopper considering its placement in a moving train, which mainly comes from the inductor [8]. The simplest way to achieve this is by operating the power devices at high switching frequencies, whereas an upper limit exists at around 1 kHz for high-power choppers when power loss is considered [9]. More specifically, at 1.5 kV catenary voltage, the typical switching frequency for 3.3-kV silicon-insulated gate bipolar transistors (Si-IGBT) modules and 3.3-kV silicon carbide-metal oxide semiconductor field effect transistor (SiC-MOSFET) is 600 Hz and 2 kHz, respectively [10], [11].

To mitigate the frequency limitations, the application of several multilevel converter topologies to reduce the inductor volume have been considered. One example is the three-level flying capacitor (TLFC) dc–dc converter that is capable of generating three voltage levels: 0, V_C, and V_{dc1} [12], [13], [14]. The TLFC can function as a multilevel bidirectional chopper with a voltage level of V_{dc1}, $V_{\mathrm{dc1}}/2$, or zero when the dc-capacitor voltage is set to half of the dc-source voltage (i.e., $V_C = V_{\mathrm{dc1}}/2$). Furthermore, if phase shift is applied to the power devices, the converter is able to produce lower maximum peak-to-peak current that is 1/4 of that produced by the CBC under the same switching frequency. While this advantage has prompted extensive researches into its possible applications in power systems and electrification of transportation modes, particularly the railway systems [15], [16], [17], the TLFC is suffering from its complex control. Specifically, the output voltage and the flying-capacitor voltage are strongly coupled, which also happens in the application of flying-capacitor converter with higher levels [18], [19], [20].

A topology that combines a CBC with multiple full-bridge converter cells as the auxiliary converter, i.e., the bidirectional chopper with an auxiliary converter (BCAC), has been reported in [21], [22], [23], [24], [25], [26], and [27], where the auxiliary converter functions as an active power filter that absorbs the ac voltage produced by the main converter. This is done by setting the switching frequency of the main converter to be equal or less than that of the auxiliary converter (i.e., $f_{\mathrm{SM}} \leq f_{\mathrm{SA}}$). It should be noted that only reactive power is processed by the auxiliary converter, and that increasing f_{SA} will also increase the ripple frequency. To further ensure the operation of the auxiliary converter as an active power filter when $V_{\mathrm{dc1}} \geq V_{\mathrm{dc2}}$, the relationship $\mathrm{N}V_C \geq V_{\mathrm{dc1}}$ must be maintained, where N represents the number of cells in the auxiliary converter, V_{dc1} and V_{dc2} are the dc-voltage sources, and V_C is the dc-capacitor voltage connected to the full-bridge cell.

The authors in [21] and [22] showed that the BCAC can reduce the switching-ripple current to 1/60 of the CBC when $N = 3$, $f_{\mathrm{SM}} = \frac{1}{4} f_{\mathrm{SA}}$, and $V_C \leq \frac{V_{\mathrm{dc1}}}{3}$. In addition, there are three

Received 4 July 2024; revised 25 October 2024 and 5 December 2024; accepted 17 December 2024. Date of publication 25 December 2024; date of current version 28 January 2025. Recommended for publication by Associate Editor M. Duffy. *(Corresponding author: Ghiffari Aby Malik Nasution.)*

The authors are with the Department of Electrical and Electronic Engineering, Institute of Science Tokyo, Meguro-ku 152-8550, Japan (e-mail: nasution.g.aa@m.titech.ac.jp; hagiwara@ee.e.titech.ac.jp).

Color versions of one or more figures in this article are available at https://doi.org/10.1109/TPEL.2024.3522332.

Digital Object Identifier 10.1109/TPEL.2024.3522332

major advantages that the BCAC holds over the CBC and TLFC. The first one is that the auxiliary converter can function as a solid-state dc circuit breaker at the low-voltage side. The second one is that the decouple of controls between the inductor current and capacitor voltage can be achieved. The third one is that there is flexibility to place the main and auxiliary converters. The last two advantages can be achieved because the main and auxiliary converters work as independent voltage sources. Furthermore, the BCAC performance under high-frequency operation has been explained in [23]. In [24], the operation of a noninverting BCAC under buck, buck-boost, and boost modes has been described. Meanwhile, the employment of the BCAC in an interleaved structure has been discussed in [25], [26], and [27], where inductor mass and volume reductions are achieved by setting $N = 3$, $M = 3$, $f_{\mathrm{SM}} = \frac{1}{4} f_{\mathrm{SA}}$, and $V_C = \frac{V_{\mathrm{dc1}}}{3}$ (M is the number of subconverters in the interleaved structure). However, due to the application of multiple cells in the auxiliary converter in these literatures, the BCAC suffers from increased power loss and potentially the cost.

The bidirectional chopper with a single-cell auxiliary converter (BCSAC), which operates under $f_{\mathrm{SM}} = f_{\mathrm{SA}}$ and $V_C = \frac{V_{dc1}}{2}$, has been proposed to reduce the produced power loss [28], [29]. By setting $N = 1$, the BCSAC is able to reduce the switching-ripple current to 4/9 of the CBC, while producing less power loss, to achieve more efficient performances than the BCAC. However, the dc-capacitor voltage control in the BCAC and BCSAC presented in [21], [22], [23], [24], [25], [26], [27], [28], and [29] cannot be achieved when the dc inductor current is zero (i.e., no power transfer between V_{dc1} and V_{dc2}). Consequently, the dc-capacitor voltage and inductor current cannot be kept at their reference values when there is no power flowing between the V_{dc1} and V_{dc2} voltage sides. In addition, the inductor volume reduction achieved by the BCSAC is limited compared to the BCAC, which prompted the need for further reduction.

To solve the control problem, this article proposes the application of ac component-based control in the inductor current and dc-capacitor controls of the BCSAC. It uses the ac component of the inductor current to regulate the dc-capacitor voltage through the auxiliary converter, which enables the achievement of the dc-capacitor voltage control when the dc inductor current is zero. To minimize the power loss produced in the chopper, the BCSAC studied in this article operates under similar settings as in [28] and [29]:

1) The frequencies of the main and auxiliary converters are the same ($f_{\mathrm{SM}} = f_{\mathrm{SA}}$);
2) The dc-capacitor voltage is half of the dc-source voltage of the high-voltage side ($V_C = \frac{V_{\mathrm{dc1}}}{2}$).

In addition, in this article, phase shift is applied to the carriers of the main and auxiliary converters, which is not the case in [28] and [29] where the two carriers are in phase. The application of phase shift is expected to mitigate the limitation on the inductor volume reduction, by further reducing the produced switching-ripple current, which consequently enables smaller inductor volume, without increasing the power loss in the chopper. As such, conducting a detailed theoretical analysis of the switching-ripple current is necessary to prove this point.

The contributions of this article can, thus, be summarized as follows.

1) Improving the stability in the BCSAC operation, especially when there is no power flowing between the voltage sources, by proposing the application of ac component-based control as a supplement to the dc component-based control. It uses the ac component of the inductor current to enable the achievement of the dc-capacitor voltage control when the dc inductor current is zero. The performances of the proposed control method under steady and transient states, along with its coordination with the conventional dc component-based control, are confirmed through experiments using a 2 kW down-scaled model.
2) Achieving further reductions on the switching-ripple current, inductor volume, and power loss, and increasing the efficiency of the BCSAC, by applying phase shift to the carriers of the main and auxiliary converters. Theoretical analysis is done on the switching-ripple current, and the results are verified through experiments. In addition, the benefits of applying phase shift in the BCSAC are validated through comparisons on the switching-ripple current, inductor volume, power loss, and efficiency between the BCSAC with phase shift (i.e., BCSAC-PS), CBC, TLFC-PS, and BCSAC with no phase shift (BCSAC-NPS).

The rest of this article is organized as follows. Section II explains the proposed chopper topology and operating principles. Section III describes the control methods, i.e., dc and ac component-based controls, applied to the main and auxiliary converters. Section IV details the theoretical analysis and comparison results on the switching-ripple current, inductor volume, and power loss and efficiency between the proposed chopper, CBC, TLFC-PS, and BCSAC-NPS. Section V presents the steady- and transient-state experimental results of the proposed chopper with the applied controls. Finally, Section VI concludes this article.

II. Circuit Configuration and Operating Principles

A. Circuit Configuration

The circuit configuration of a bidirectional chopper with a single-cell auxiliary converter (BCSAC) is given in Fig. 1(a). The BCSAC is formed by a CBC as the main converter, a full-bridge cell equipped with a floating dc-capacitor as the auxiliary converter, and an inductor. The main converter is linked to two dc-voltage sources, V_{dc1} and V_{dc2}, where the former shows the high-voltage-side voltage and the latter shows the low-voltage-side voltage, while v_M shows the low-voltage-side voltage of the main converter. S_1 and S_2 show the upper and lower switching devices of the main converter, respectively. The auxiliary converter is connected in series with the main converter and the inductor. v_A shows the auxiliary converter voltage and v_C shows the dc-capacitor voltage, where the relationship $V_C = \frac{V_{dc1}}{2}$ holds for its dc component to reduce the voltage rating of the power devices used in the auxiliary converter, which consequently reduces the produced conduction loss. v_L shows the inductor voltage and i_L shows the inductor current. S_3 and

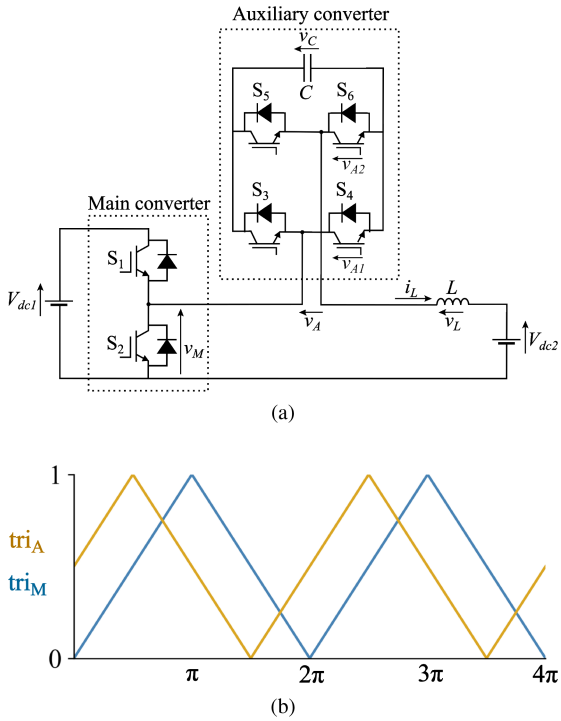

Fig. 1. Proposed bidirectional chopper with single-cell auxiliary converter. (a) Circuit configuration. (b) Carrier waveforms.

S_4 show the upper and lower switching devices of one leg of the auxiliary converter that is connected to the main converter, respectively, and v_{A1} shows the low-voltage-side voltage of the leg. Meanwhile, S_5 and m_6 show those of another leg that is connected to the inductor, and v_{A2} shows the low-voltage-side voltage of the leg. It should be noted that the parameters of the BCSAC are designed for BESS application in electric railways in this article, i.e., they are applicable for LVDC or MVDC systems.

The triangular carrier waveforms applied to the main and auxiliary converters, tri_M and tri_A, respectively, are given in Fig. 1(b), where tri_A leads tri_M by 90°. Meanwhile, the relationship $f_{\text{SM}} = f_{\text{SA}}$ is held to minimize the produced switching loss, where f_{SM} shows the frequency of tri_M, while f_{SA} shows that of tri_A. In the auxiliary converter, the equivalent switching frequency of v_A is $2f_{\text{SA}}$, as the result of the application of unipolar pulsewidth modulation (PWM).

B. Operating Principles

Fig. 2 shows an example of the ideal voltage and current waveforms of the BCSAC. When the deadtime in the main converter (i.e., brief time interval where both S_1 and S_2 are OFF) is zero, v_M is given by

$$v_M = \begin{cases} V_{\text{dc1}} & (S_1\text{: ON}, S_2\text{: OFF}) \\ 0 & (S_1\text{: OFF}, S_2\text{: ON}). \end{cases} \tag{1}$$

Furthermore, v_M has both the dc component, $(v_M)_{\text{dc}}$, and the ac component, $(v_M)_{\text{ac}}$, which can be determined by

$$(v_M)_{\text{dc}} = d_M V_{\text{dc1}} \tag{2}$$

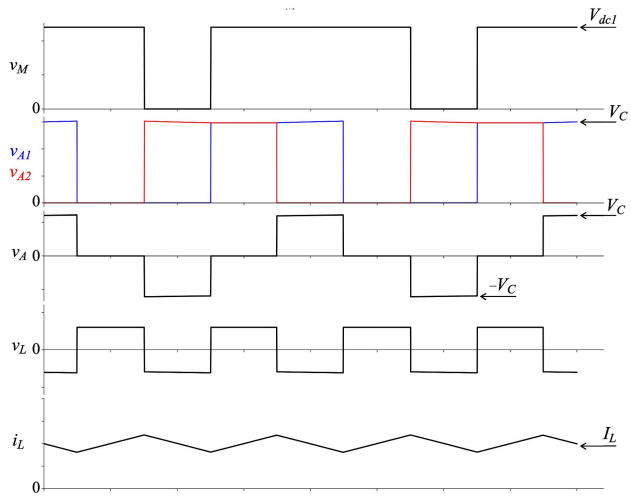

Fig. 2. Example of the ideal voltage and current waveforms of the BCSAC.

$$(v_M)_{\text{ac}} = \begin{cases} (1-d_M)V_{\text{dc1}} & (S_1\text{: ON}, S_2\text{: OFF}) \\ -d_M V_{\text{dc1}} & (S_1\text{: OFF}, S_2\text{: ON}) \end{cases} \tag{3}$$

where d_M is the duty ratio of S_1. Meanwhile, when the deadtimes in the auxiliary converter (i.e., brief time intervals where both S_3 and S_4 (S_5 and S_6) are OFF) are zero, v_{A1} and v_{A2} are given by

$$v_{A1} = \begin{cases} V_C & (S_3\text{: ON}, S_4\text{: OFF}) \\ 0 & (S_3\text{: OFF}, S_4\text{: ON}) \end{cases} \tag{4}$$

$$v_{A2} = \begin{cases} V_C & (S_5\text{: ON}, S_6\text{: OFF}) \\ 0 & (S_5\text{: OFF}, S_6\text{: ON}) \end{cases} \tag{5}$$

where $v_A = v_{A1} - v_{A2}$.

In the BCSAC, the role of the auxiliary converter is to produce the ac component, $(v_A)_{\text{ac}}$, that is equivalent to that of the main converter (i.e., $(v_A)_{\text{ac}} = (v_M)_{\text{ac}}$), so that the ac component in the inductor can be reduced to zero. From (3), $(v_M)_{\text{ac}}$ has the maximum value of V_{dc1} and the minimum value of $-V_{\text{dc1}}$. Consequently, $(v_A)_{\text{ac}}$ has the same maximum and minimum values as $(v_M)_{\text{ac}}$, where the relationship $V_C \geq V_{\text{dc1}}$ should be satisfied so that the auxiliary converter is able to work as an active power filter under all conditions when $V_{\text{dc1}} \geq V_{\text{dc2}}$. On the other hand, the dc-capacitor voltage is set to $V_C = \frac{V_{\text{dc1}}}{2}$ in this article because of the reasons mentioned in the previous section. As a result, a dc component may occur in v_A if the auxiliary converter attempts to produce the ac voltage $(v_M)_{\text{ac}}$ given in (3), due to overmodulation in the converter.

To solve this problem, normalization should be applied to $(v_A)_{\text{ac}}$, where its maximum and minimum values should be limited to $0.5V_{\text{dc1}}$ and $-0.5V_{\text{dc1}}$, respectively. For example, the relationship $(v_M)_{\text{ac}} \geq 0.5V_{\text{dc1}}$ always holds under $0 \leq d_M < 0.5$, when S_1 is ON and S_2 is OFF. Thus, the value of $(v_A)_{\text{ac}}$ is set to $0.5V_{\text{dc1}}$ under the said condition. Furthermore, in a single switching period, $(v_A)_{\text{ac}}$ should average zero. Under these considerations, $(v_A)_{\text{ac}}$ when $0 \leq d_M < 0.5$ can be determined

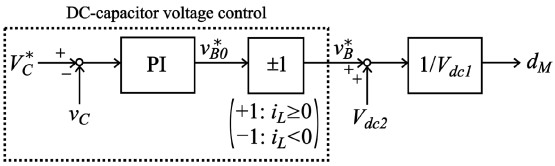

Fig. 3. Block diagram of the main converter control using DC component-based control.

by

$$(v_A)_{\rm ac} = \begin{cases} 0.5V_{\rm dc1} & (S_1\text{: ON}, S_2\text{: OFF}) \\ -d_M V_{\rm dc1} & \\ +\frac{{d_M}^2 - 0.5d_M}{d_M - 1} V_{\rm dc1} & (S_1\text{: OFF}, S_2\text{: ON}). \end{cases} \tag{6}$$

Similarly, $(v_A)_{\rm ac}$ when $0.5 \leq d_M \leq 1$ can be determined by

$$(v_A)_{\rm ac} = \begin{cases} (1 - d_M)V_{\rm dc1} & \\ +\frac{{d_M}^2 - 1.5d_M + 0.5}{d_M} V_{\rm dc1} & (S_1\text{: ON}, S_2\text{: OFF}) \\ -0.5V_{\rm dc1} & (S_1\text{: OFF}, S_2\text{: ON}). \end{cases} \tag{7}$$

From (3), (6), and (7), when $d_M = 0.5$, the relationship $(v_A)_{\rm ac} = (v_M)_{\rm ac}$ is satisfied. As a result, the frequency component of $f_{\rm SM}$ contained in $(v_M)_{\rm ac}$ is canceled out by the auxiliary converter so that no frequency component of $f_{\rm SM}$ exists in the inductor current. On the other hand, when $d_M \neq 0.5$, the relationship $(v_A)_{\rm ac} = (v_M)_{\rm ac}$ is not satisfied, meaning that there exists the frequency component of $f_{\rm SM}$ in the inductor current.

III. Control Method

Based on the components used, the control method of the BCSAC-PS can be divided into dc component-based control and ac component-based control. The dc component-based control, that has been presented in [21], [22], [23], [24], [25], [26], [27], [28], and [29], is applied when the dc inductor current is not zero. Similar to [28], [29], the main converter is responsible for the dc-capacitor voltage control, while the auxiliary converter is used to achieve the dc current control, which could improve the current controllability. On the other hand, the ac component-based control proposed in this article is used when the dc inductor current is zero, where the main converter is responsible for the dc current control and the auxiliary converter is used to achieve the dc-capacitor voltage control. In addition, this article uses the average value of the actual dc current in the inductor current control, that is not the case in [21], [22], [23], [24], [25], [26], [27], [28], and [29], which would improve the control accuracy and stability because the effect of switching-ripple component can be eliminated.

A. DC Component-Based Control

Fig. 3 shows the block diagram of the main converter control when dc component-based control is used, where the main converter function is to regulate the dc-capacitor voltage. More specifically, the traditional PI control is applied to produce the voltage reference v^*_{B0} based on the difference between the actual dc-capacitor voltage, v_C, and its reference value, V^*_C. Depending on the value of the inductor current, i_L, the polarity of v^*_{B0} can alternate between positive and negative, as shown in Fig. 3. For example, when $V^*_C > v_C$, the resulted v^*_B is as follows:

$$v^*_B = \begin{cases} v^*_{B0} & (i_L > 0) \\ -v^*_{B0} & (i_L < 0). \end{cases} \tag{8}$$

Furthermore, $V_{\rm dc2}$ is added to v^*_B as a feedforward control, which is then normalized by $V_{\rm dc1}$. Finally, the duty ratio of S_1, d_M, is obtained as

$$d_M = \frac{v^*_B + V_{\rm dc2}}{V_{\rm dc1}} \tag{9}$$

with a maximum value of $+1$ and a minimum value of zero.

To clearly illustrate the dc-capacitor voltage control in Fig. 3, a positive dc inductor current (i.e., $i_L = I_L > 0$) is assumed to flow in the circuit. Based on (2) and (9), the dc power at the low-voltage side of the main converter is obtained as $(v_M)_{\rm dc} I_L = d_M V_{\rm dc1} I_L = (v_B + V_{\rm dc2}) I_L$. Here, v_B is the actual voltage used in the dc-capacitor voltage control, and the relationship $v_B = v^*_B$ is assumed to hold. When $V^*_C = v_C$, the dc power at the low-voltage sides of the main converter and the chopper are the same (i.e., $(v_M)_{\rm dc} I_L = V_{\rm dc2} I_L$), because $v_B = 0$. In this case, there is no power flowing in the auxiliary converter. Meanwhile, when $V^*_C > v_C$, a positive v^*_B occurs as given in Fig. 3. Consequently, a positive power is formed between v_B and I_L, and it is superimposed on $(v_M)_{\rm dc} I_L$. As a result, the relationship $(v_M)_{\rm dc} I_L > V_{\rm dc2} I_L$ holds in the circuit, where this power will be received by the auxiliary converter through the production of v^*_B (given in Fig. 4). Consequently, a positive power $V_{\rm dc2} I_L$ flows into the auxiliary converter and v_C rises, which means that all the additional power superimposed on the main converter flows in the auxiliary converter. The decouple of controls between the dc-capacitor voltage and the dc inductor current can be achieved because the voltage component v^*_B produced by the main and auxiliary converters cancel each other out.

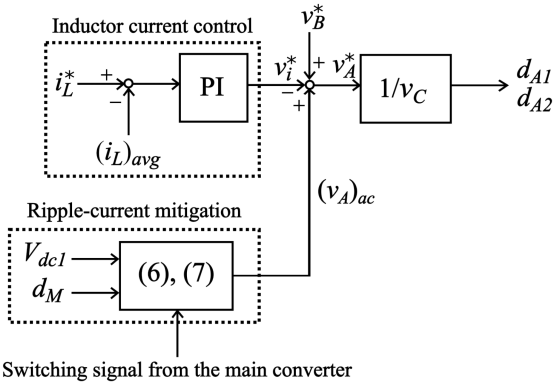

Fig. 4. Block diagram of the auxiliary converter control using DC component-based control.

Fig. 4 shows the block diagram of the auxiliary converter control when dc component-based control is used, where the auxiliary converter control has the following functions: 1) Regulation of the dc inductor current, and 2) Mitigation of the ripple current. The traditional PI control is applied in the dc

inductor current control to produce the voltage command v_i^* based on the difference between its actual dc average value, $(i_L)_{\text{avg}}$, and its reference value, i_L^*. $(i_L)_{\text{avg}}$ is obtained by applying a moving-average filter with a frequency of f_{SM} to i_L, with the sampling frequency of $4f_{\text{SM}}$, where the sampling is done at the peaks and bottoms of tri_{M} and tri_{A}. It should be noted that the time delay originating from the moving-average filter application of 5 kHz ($= 200\ \mu$s) is much smaller than the response speed of the dc inductor current control (i.e., more than a few milliseconds). Thus, the effect of applying moving-average filter to the stability and dynamic response is negligible as long as f_{SM} is high enough. Furthermore, $(v_A)_{\text{ac}}$, that is obtained from (6) and (7), and the voltage reference produced by the main converter control, v_B^*, are added to v_i^* as a feedforward control, producing v_A^* as the voltage reference of the auxiliary converter. After the normalization of v_A^* by v_C, the duty ratio of S_3, d_{A1}, and that of S_5, d_{A2}, are obtained with a maximum value of $+1$ and a minimum value of -1. Finally, the produced d_{A1} and d_{A2} have to be normalized to have a maximum value of $+1$ and a minimum value of zero. Thus, these values are compared with tri_{A}, which has a maximum value of $+1$ and a minimum value of zero.

The traditional PI control is used in both converters, where the transfer functions in the Laplace domain for the dc-capacitor voltage and inductor current controls are given as

$$\frac{v_C}{V_C^*} = \frac{sK_{\text{vp-dc}}i_L + K_{\text{vi-dc}}i_L}{(v_C)_{\text{dc}}Cs^2 + sK_{\text{vp-dc}}i_L + K_{\text{vi-dc}}i_L} \tag{10}$$

$$\frac{i_L}{i_L^*} = \frac{sK_{\text{ip-dc}} + K_{\text{ii-dc}}}{Ls^2 + sK_{\text{ip-dc}} + K_{\text{ii-dc}}} \tag{11}$$

where C shows the capacitance value of the dc-capacitor and $(v_C)_{\text{dc}}$ shows the dc component of the dc-capacitor voltage. $K_{\text{vp-dc}}$ and $K_{\text{vi-dc}}$ show the proportional and integral gains of the dc-capacitor voltage control in the dc component-based control, while $K_{\text{ip-dc}}$ and $K_{\text{ii-dc}}$ show those of the inductor current control, and their values are appropriately set. It is evident from (10) that stable control of the dc-capacitor voltage cannot be achieved when $i_L = 0$ A.

It is necessary to note the difference between v_B^* and v_i^* in the dc component-based control. Assuming that there is no power loss in the converter, the relationship $v_B^* = 0$ holds under the steady state. On the other hand, $v_i^* \neq 0$ holds under the same condition. The reason is that an amount of dc voltage occurs in v_A due to the PWM, which should be canceled by v_i^* to achieve the dc current control. In other words, a dc component occurs in v_i^* to make the average value of v_A in one switching period be zero. It should also be noted that the value of v_i^* will have an effect on the switching-ripple current, as will be explained in the section on theoretical analysis.

B. AC Component-Based Control

Fig. 5 shows the block diagram of the main converter control when ac component-based control is used, where the main converter function is to regulate the dc inductor current. The traditional PI control is applied to produce the voltage command v_i^* based on the difference between the average (i.e., dc) inductor current value, $(i_L)_{\text{avg}}$, and its reference value, i_L^*. The voltage command v_i^* and V_{dc2} are summed up, and normalized by V_{dc1} to obtain d_M with a maximum value of $+1$ and a minimum value of zero

$$d_M = \frac{v_i^* + V_{\text{dc2}}}{V_{\text{dc1}}}. \tag{12}$$

Fig. 6(a) shows the block diagram of the auxiliary converter control when ac component-based control is used, where it differs from Fig. 3 in that the ac inductor current with a frequency of f_{SM} is intentionally controlled to achieve the dc-capacitor voltage control. Fig. 6(b) shows the ideal waveforms when $V_C^* > v_C$, where $(i_L)_{\text{ac}}$ is the ac current included in i_L with only f_{SM} frequency component that is produced by v_B^*. In Fig. 6(a), the traditional PI control is used to produce voltage reference v_{B0}^* based on the difference between the actual dc-capacitor

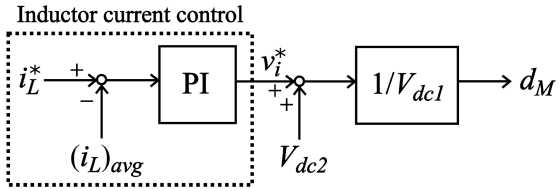

Fig. 5. Block diagram of the main converter control using AC component-based control.

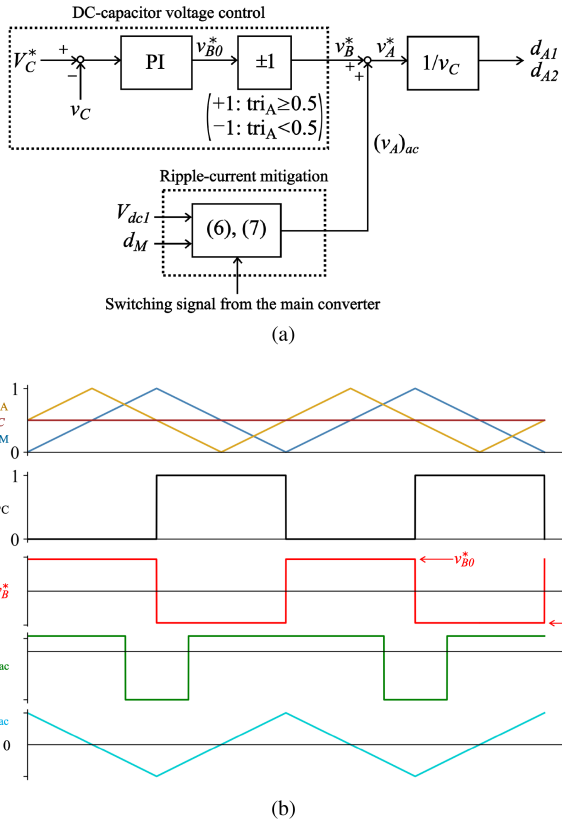

Fig. 6. Auxiliary converter control using AC component-based control: (a) Block diagram, and (b) ideal waveforms when $V_C^* > v_C$ and only frequency component f_{SM} is assumed in $(i_L)_{\text{ac}}$.

voltage, v_C, and its reference value, V_C^*, where the polarity of v_B^* is changed based on the triangular carrier waveform of the auxiliary converter, tri_A. It is further normalized by v_C, producing d_{A1} and d_{A2} with a maximum value of $+1$ and a minimum value of -1. Similarly, d_{A1} and d_{A2} are again normalized to have a maximum value of $+1$ and a minimum value of zero, followed by the comparison with tri_A.

Meanwhile, the transfer functions in the Laplace domain for the dc-capacitor voltage and inductor current controls using ac component-based control are given as

$$\frac{i_L}{i_L^*} = \frac{sK_{\text{ip-ac}} + K_{\text{ii-ac}}}{Ls^2 + sK_{\text{ip-ac}} + K_{\text{ii-ac}}} \tag{13}$$

$$\frac{v_C}{V_C^*} = \frac{sK_{\text{vp-ac}}Y + K_{\text{vi-ac}}Y}{(v_C)_{\text{dc}}\,Cs^2 + sK_{\text{vp-ac}}Y + K_{\text{vi-ac}}Y} \tag{14}$$

where C shows the capacitance value of the dc-capacitor, Y shows a constant produced from $(v_A)_{\text{ac}}$ and $(i_L)_{\text{ac}}$, and $(v_C)_{\text{dc}}$ shows the dc component of the dc-capacitor voltage. $K_{\text{vp-ac}}$ and $K_{\text{vi-ac}}$ show the proportional and integral gains of the dc-capacitor voltage control in the ac component-based control, while $K_{\text{ip-ac}}$ and $K_{\text{ii-ac}}$ show those of the inductor current control. It is evident from (14) that the dc-capacitor voltage control can be achieved regardless of the value of i_L. Thus, the supplementary application of ac component-based control can contribute to the stability improvement of the BCSAC operation when $i_L = 0$ A.

To give a clearer image on v_B^* polarity, let S_C given in Fig. 6(b) be the PWM signal produced from the comparison of tri_A with a duty ratio $d_C = 0.5$. Specifically, $S_C = 1$ when $\text{tri}_\text{A} < d_C$ and $S_C = 0$ when $\text{tri}_\text{A} \geq d_C$. Based on S_C, v_B^* is given by

$$v_B^* = \begin{cases} -v_{B0}^* & (S_\text{C}\text{: } 1) \\ v_{B0}^* & (S_\text{C}\text{: } 0) \end{cases} \tag{15}$$

where v_{B0}^* is the output of the PI control, and summed by the $(v_A)_{\text{ac}}$ obtained from (6) and (7) to produce the voltage reference v_A^*. From Fig. 6(b) and (15), v_A^* can be determined by

$$v_A^* = \begin{cases} -v_B^* + (v_A)_{\text{ac}} & (\text{tri}_\text{A} < d_C) \\ v_B^* + (v_A)_{\text{ac}} & (\text{tri}_\text{A} \geq d_C). \end{cases} \tag{16}$$

In Fig. 6(b), $(i_L)_{\text{ac}}$ is a triangular waveform with a frequency component of f_{SM} that is produced by v_B^*. It should be noted that $(i_L)_{\text{ac}}$ can be either in phase or out of phase with $(v_A)_{\text{ac}}$, depending on the relationship between V_C^* and v_C.

To further explain the dc-capacitor voltage control, the relationship $V_C^* > v_C$ is assumed in the auxiliary converter. Based on Fig. 6(a), a positive v_{B0}^* is generated, leading to the production of $(i_L)_{\text{ac}}$ that is in phase with $(v_A)_{\text{ac}}$, as shown in Fig. 6(b). As a result, a positive power $(v_A)_{\text{ac}}(i_L)_{\text{ac}}$ is formed, which flows into the capacitor and increases v_C.

IV. Theoretical Analysis and Comparison

The objective in applying phase shift to the BCSAC is to further reduce the switching-ripple current, which will correspondingly reduce the inductor volume and potentially the power loss in the converter. To evaluate the achievement of that objective, theoretical comparisons on the switching-ripple current, inductor volume, power loss, and efficiency are carried out between the BCSAC-PS (i.e., BCSAC-PS), CBC, TLFC-PS, and BCSAC without phase shift (i.e., BCSAC-NPS). The circuit configurations of the CBC and TLFC-PS are given in Fig. 7(a) and (b), respectively. It should be noted, however, that cost comparison falls outside the scope of this article, and should be deferred for future research.

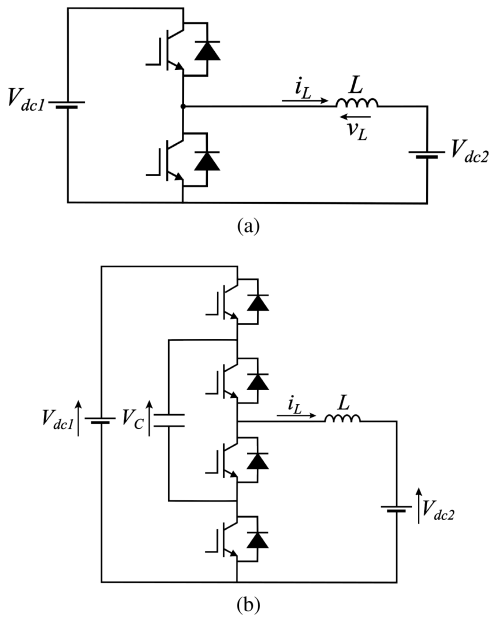

Fig. 7. Circuit configuration of (a) CBC, and (b) TLFC DC–DC converter.

A. Switching-Ripple Current

Theoretical analysis on the switching-ripple current of the BCSAC-PS is conducted using similar approaches as in [29], where the following assumptions are applied in the analysis.

1) Steady-state operation with no power loss is considered, meaning that the voltage reference used in the dc-capacitor voltage control is zero ($v_B^* = 0$).
2) There is no deadtime in the main and auxiliary converters, which is valid when the switching period of the chopper is sufficiently longer than the deadtime period. Deadtime here is defined as the brief intervals where complementary switches (i.e., S_1 and S_2, S_3, and S_4, and S_5 and S_6) are OFF.
3) The dc-capacitor voltage is set to $V_C = \frac{V_{\text{dc1}}}{2}$ and its ac component is zero.

Under the second condition, the value of d_M is determined by

$$d_M = \frac{V_{\text{dc2}}}{V_{\text{dc1}}}. \tag{17}$$

The theoretical analysis is conducted under two different ranges of d_M, i.e., $0 \leq d_M < 0.5$ and $0.5 \leq d_M \leq 1$, where the analysis under $0 \leq d_M < 0.5$ is given in the Appendix. Based on the analysis results, the switching-ripple current, I_{ripple}, under

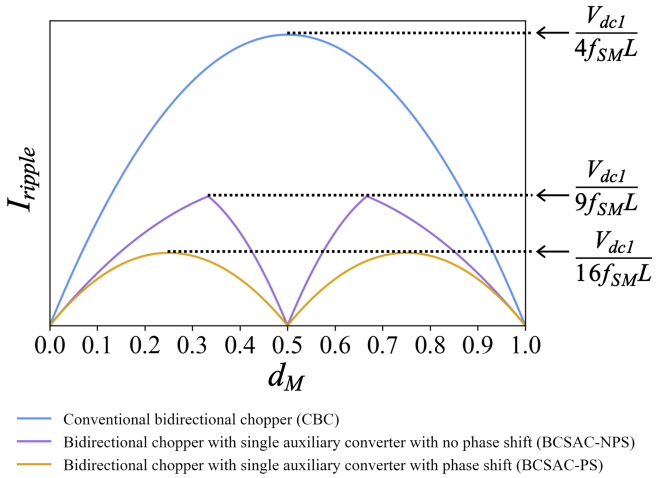

Fig. 8. Theoretical waveforms of switching-ripple current.

$0 \leq d_M < 0.5$ is given by

$$I_{\text{ripple}} = \frac{V_{\text{dc1}}}{2f_{\text{SM}}L}(1-2d_M)d_M \tag{18}$$

while I_{ripple} under $0.5 \leq d_M \leq 1$ is given by

$$I_{\text{ripple}} = \frac{V_{\text{dc1}}}{2f_{\text{SM}}L}(2d_M-1)(1-d_M). \tag{19}$$

Based on (18) and (19), the maximum value of I_{ripple} can be obtained when $d_M = 1/4$ and $d_M = 3/4$, respectively, as

$$(I_{\text{ripple}})_{\text{max}} = \frac{V_{\text{dc1}}}{16f_{\text{SM}}L}. \tag{20}$$

Meanwhile, $(I_{\text{ripple}})_{\text{max}}$ for the BCSAC-NPS can be obtained from [28], [29] as

$$(I_{\text{ripple}})_{\text{max}} = \frac{V_{\text{dc1}}}{9f_{\text{SM}}L} \tag{21}$$

Furthermore, $(I_{\text{ripple}})_{\text{max}}$ for the CBC can be obtained as

$$(I_{\text{ripple}})_{\text{max}} = \frac{V_{\text{dc1}}}{4f_{\text{SM}}L}. \tag{22}$$

Based on (20) and (22), the BCSAC-PS is able to reduce the switching-ripple current to 1/4 of the CBC. This is significantly lower than that produced by the BCSAC-NPS, that is 4/9 of the CBC [from (21) and (22)]. The theoretical waveforms of the ripple current are given in Fig. 8, where the horizontal axis shows the value of d_M and the vertical axis shows I_{ripple}. The switching-ripple currents of the CBC, BCSAC-NPS, and BCSAC-PS are shown by the blue, purple, and gold lines, respectively. Fig. 8 shows that there is a symmetry between the switching-ripple current of the BCSAC-PS under $d_M < 0.5$ and $d_M > 0.5$, similar to that of the BCSAC-NPS, and that the advantage of BCSAC-PS over the CBC is especially apparent when the operating duty ratio is around $d_M = 0.5$.

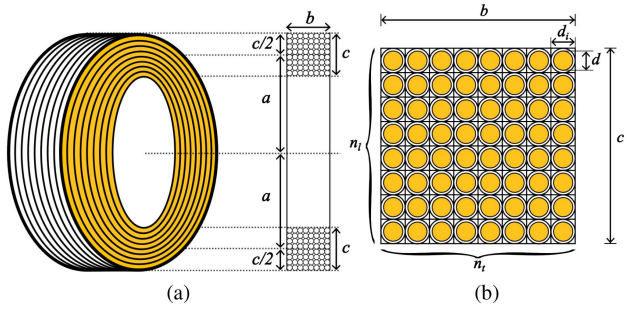

Fig. 9. Dimensions of (a) air-core inductor, and (b) rectangular cross-section.

TABLE I
PARAMETERS OF THE AIR-CORE INDUCTORS

Parameter	CBC	BCSAC-NPS	TLFC-PS/BCSAC-PS
L	0.9 mH	0.4 mH	0.225 mH
a	27.62 cm	23.78 cm	16.91 cm
b	15.6 cm	13 cm	13 cm
c	18.2 cm	15.6 cm	15.6 cm
d	25.23 mm	25.23 mm	25.23 mm
d_i	26 mm	26 mm	26 mm
n_t	6	5	5
n_l	7	6	6
n	42	30	30
v_L	66.09 dm^3	40.73 dm^3	24.94 dm^3

B. Inductor Volume

Theoretical analysis on inductor volume of the four choppers is conducted based on the method described in [29] and [30], where the following assumptions are used in the analysis.

1) Air-core inductors are used.
2) Brooks coil geometry is adopted in the inductors.
3) The inductors have a maximum current capacity, I_{max}, of 1000 A and a maximum current density, J_{max}, of 2×10^6 A/m^2.
4) Under the same switching frequency, the same amount of ripple current should be produced by all choppers.

Air-core inductors are employed because they are widely used in chopper for electric railways due to their characteristics that show better size reduction in higher operating frequencies, nonexistent core saturation, and produce no iron loss [31], [32], [33]. In addition, Brooks coil geometry is assumed in the inductors to attain the maximum achievable inductance value for a specified length of wire [30]. The air-core inductor dimensions with its rectangular cross-section are given in Fig. 9, where a is the distance between the axis of the winding and that of the inductor, b is the width of the winding cross-section, c is the height of the winding cross-section, d is the diameter of the wire without the insulation coating, d_i is the diameter of the wire with the insulation coating, n_l is the number of layers, n_t is the number of turns per layer, and n is the number of turns.

Based on the assumed I_{max} and J_{max}, the other parameters of the inductor are calculated by following the same calculation methods as those described in [29], where the simplified flowchart of the calculation process is shown in Fig. 10. The resulted parameters of the air-core inductors used in the four choppers are given in Table I. The inductance value for each

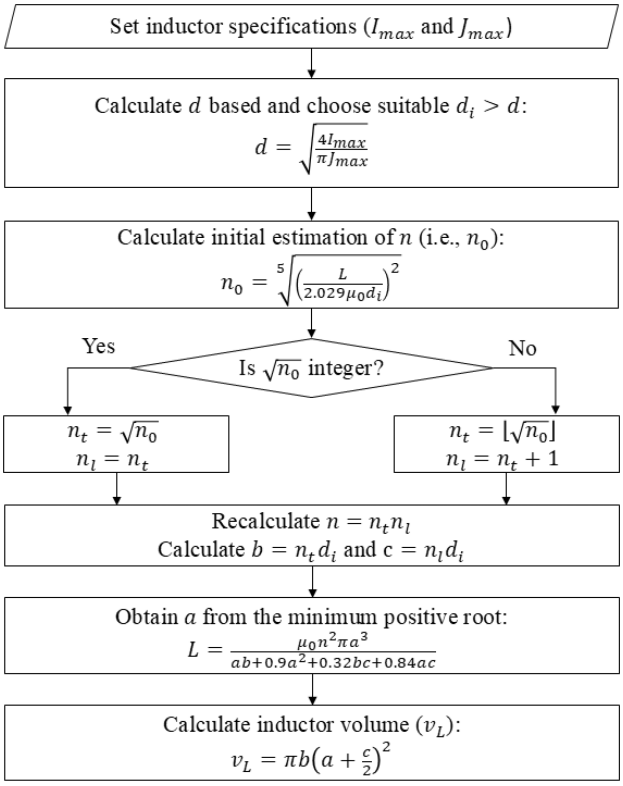

Fig. 10. Simplified flowchart of the inductor volume calculation process.

chopper is set to $L = 0.9$ mH for the CBC, $L = 0.225$ mH for the TFLC and BCSAC-PS, and $L = 0.4$ mH for the BCSAC, where the values are determined by considering the fourth condition set in the analysis and the theoretical results of the switching-ripple current analysis. Based on the results, the BCSAC-PS is able to reduce the inductor volume by 62.3% compared to that of the CBC. The achieved reduction is comparably larger than that achieved by the BCSAC-NPS (i.e., 38.4%). Furthermore, this reduction is comparable to that achieved by the TLFC-PS.

To further confirm the significance of the inductor volume reduction achieved by the BCSAC-PS related to its additional components, theoretical analysis on the total chopper volume is conducted. In the analysis, the dc film capacitor E50.N15-323NT0 from Electronicon ($C = 32\ \mu$F, $I_{\max} = 50$ A) is chosen, where a parallel connection of twenty capacitors is used in the auxiliary converter to account for the assumed $I_{\max}$ in the inductor volume analysis, giving an equivalent capacitance value of 0.64 mF. Furthermore, based on the required voltage ratings in actual applications, the insulated gate bipolar transistors (IGBT) power module 1MBI1000UG-330 from Fuji Electric (Si-IGBT, 1-in-1, 3.3 kV) is selected, and two modules are used in each of the CBC, TLFC-PS, and the main converter of the BCSAC-NPS and BCSAC-PS. In addition, the IGBT power module CM1000DX-24T from Mitsubishi Electric (Si-IGBT, 1-in-1, 1.2 kV) is selected for the TLFC-PS, BCSAC, and BCSAC-PS. The TLFC-PS uses two modules, while each of the BCSAC-NPS and BCSAC-PS uses four modules in their full-bridge auxiliary converter. The volume of these components is estimated based on the dimensions provided in [34], [35], and [36].

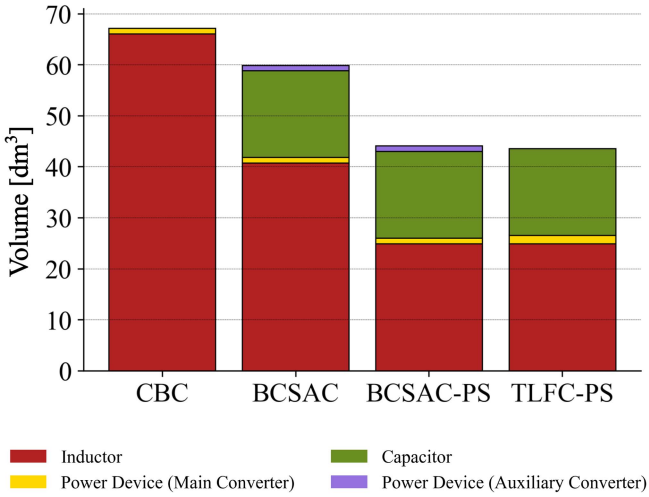

Fig. 11. Volume breakdown of the four choppers.

TABLE II
PARAMETERS USED IN THE POWER LOSS AND EFFICIENCY ANALYSIS

Rated power	P	1.5 MW
DC-voltage source 1	$V_{\text{dc}1}$	1.5 kV
DC-voltage source 2	$V_{\text{dc}2}$	0.45 and 1.05 kV
Switching frequency (main converter)	f_{SM}	5 kHz
Switching frequency (auxiliary converter)	f_{SA}	5 kHz
Switching frequency (TLFC-PS)	f_{TLFC}	5 kHz
Inductance (CBC)	L	0.9 mH
Inductance (TLFC-PS, BCSAC-PS)	L	0.225 mH
Inductance (BCSAC-NPS)	L	0.4 mH
DC-capacitor voltage (TLFC-PS, BCSAC-NPS, BCSAC-PS)	V_C	0.75 kV

The volume breakdown of the four choppers, which consists of the inductor, and the capacitor and power devices in both the main and auxiliary converters, is given in Fig. 11. The results show that the total volume of the BCSAC-PS is 34.4% lower than that of the CBC. This is because the achieved inductor volume reduction (41.15 dm^3) is significantly higher than the combined volume of the additional components that come with the auxiliary converter, i.e., the capacitors (17.02 dm^3) and the power devices (1.04 dm^3). Furthermore, the total volume of the BCSAC-PS is similar to that the TLFC-PS.

C. Power Loss and Efficiency

Theoretical analysis of the power loss and efficiency conducted on the four choppers is done under the following settings, which are listed in Table II.

1) For all choppers, the rated power is set to $P = 1.5$ MW, where the high-voltage-side voltage is set to $V_{\text{dc}1} = 1.5$ kV, which is within the typical range of dc voltage supply of electric railway systems [37].
2) The low-voltage-side voltage, $V_{\text{dc}2}$, is alternated between 0.45 and 1.05 kV to change the value of d_M based on (17).

3) For all choppers, the switching frequency is set at $f_{SM} = f_{SA} = f_{TLFC} = 5$ kHz. It should be noted that the equivalent switching frequency of the TLFC-PS is $2f_{TLFC}$, due to the application of phase shift.
4) The inductance values are set to be the same as in the inductor volume analysis, i.e., $L = 0.9$ mH for the CBC, $L = 0.225$ mH for the TFLC and BCSAC-PS, and $L = 0.4$ mH for the BCSAC-NPS.
5) For the TLFC-PS, BCSAC-NPS, and BCSAC-PS, the dc-capacitor voltage is set to be half of V_{dc1} (i.e., $V_C = 0.75$ kV).

Furthermore, the analysis considers the conduction losses, the switching loss, and the reverse recovery loss of the IGBT and free-wheeling diode, and the inductor loss, where the formula can be commonly found in [38], [39], [40], and [41], while the loss and efficiency calculations follow the same methods as those described in [29]. Based on the required voltage rating, the same power devices as that in the inductor volume analysis are used, and the losses are calculated using approximations based on the specifications of both IGBT modules listed in [35] and [36].

The power losses breakdown of the four choppers under $d_M = 0.3$ and $d_M = 0.7$ are given in Fig. 12. Under the maximum power rating, the CBC produces around 7.7 kW of power loss in average. The largest contributor is the conduction loss with 3.1 kW, followed by inductor loss at 2.6 kW and switching loss at 2 kW. Comparatively, both the TLFC-PS and BCSAC-NPS produce larger power losses. The TLFC-PS power loss is around 8.9 kW, where the majority similarly comes from the conduction loss at 5.3 kW and switching loss at 2.5 kW, while the inductor loss gives 1.1 kW. Meanwhile, the BCSAC-NPS loses around 11.7 kW of power. The total losses in the main and auxiliary converters are similar, where the former produces 5.1 kW and the latter produces 5 kW. On the other hand, the BCSAC-PS has around 11.04 kW of power loss, which is comparatively larger than the CBC and TLFC-PS, but less than the BCSAC-NPS. The loss reduction comes from the smaller inductor loss and the switching loss of the auxiliary converter (i.e., 1.1 kW and 0.4 kW, respectively), compared with those produced by the BCSAC-NPS (i.e., 1.6 kW and 0.6 kW, respectively). In general, the common biggest power loss contributor across the four choppers is the conductor loss.

Based on the power loss analysis results, the efficiencies of all choppers are calculated. Fig. 13 shows the efficiency comparison, where the CBC is shown in blue line, the TLFC-PS is shown in green line, the BCSAC-NPS is shown in purple line, and the BCSAC-PS is shown in gold line. When $d_M = 0.3$, the BCSAC-PS can achieve an average performance of 98%, which is lower than the efficiencies of CBC and TLFC-PS at 98.7% and 98.4%, respectively, but slightly higher than the efficiency of BCSAC-NPS at 97.9%. Similarly, when $d_M = 0.7$, the BCSAC-PS can achieve an average performance of 99.1%, which is lower than the efficiencies of CBC and TLFC-PS at 99.4% and 99.3%, respectively, but slightly higher than the efficiency of BCSAC-NPS at 99%. It should be noted that the efficiency differences between the four choppers become smaller as the d_M increases. Furthermore, the efficiencies for all choppers are the highest when the power rating is 75 kW, where the current is $i_L = 250$ A, for both d_M values.

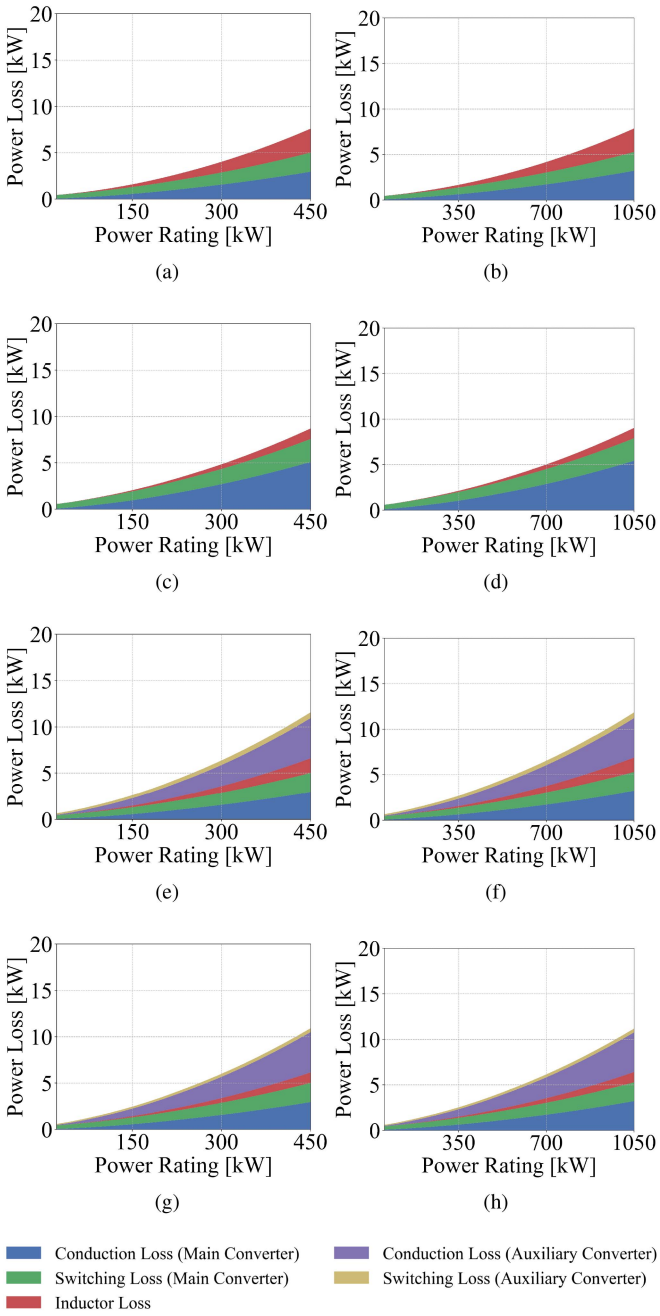

Fig. 12. Loss breakdown of (a) CBC when $V_{dc2} = 0.45$ kV, (b) CBC when $V_{dc2} = 1.05$, kV (c) TLFC-PS when $V_{dc2} = 0.45$ kV, (d) TLFC-PS when $V_{dc2} = 1.05$ kV, (e) BCSAC-NPS when $V_{dc2} = 0.45$ kV, (f) BCSAC-NPS when $V_{dc2} = 1.05$ kV, (g) BCSAC-PS when $V_{dc2} = 0.45$ kV, (h) BCSAC-PS when $V_{dc2} = 1.05$ kV.

Overall, the BCSAC-PS produces significantly lower switching-ripple current than the CBC and BCSAC-NPS, which allows the application of smaller inductor, while also producing lower power loss than the BCSAC-NPS. Although the BCSAC-PS efficiency is still lower than those of the CBC and TLFC-PS, the difference is not significant when the inductor volume reduction is considered. For example, if the inductor volume reduction

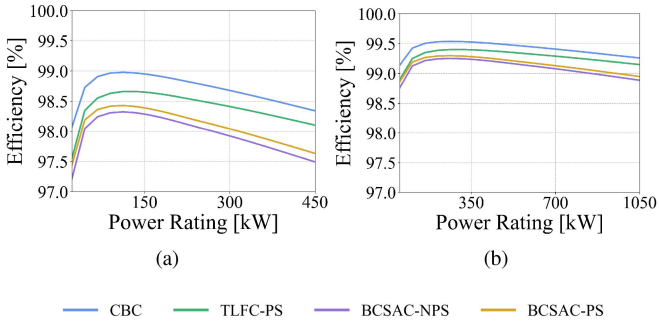

Fig. 13. Efficiency of the four choppers when (a) $V_{\text{dc2}} = 0.45$ kV ($d_M = 0.3$), and (b) $V_{\text{dc2}} = 1.05$ kV ($d_M = 0.7$).

is further translated into inductor mass reduction, then the body mass of the vehicle can be reduced, as has been shown in [24]. In the bigger picture, this could potentially give positive impact to the energy efficiency of the vehicle by reducing the required energy to move it. However, mass analysis is outside the scope of this article.

For example, the inductor volume reduction could reduce the total energy required to move the vehicle, which could potentially give positive impact to the energy efficiency of the vehicle in the bigger picture.

V. Experiment

A. Experimental Conditions

To validate the performance of the controls (i.e., dc and ac component-based controls) and operation of the BCSAC-PS, a 2 kW down-scaled experimental model is used, which is given in Fig. 14. The model is configured as follows.

1) The dc-power supplies KIKUSUI PAT160-50T and HEADSPRING biATLAS-5D525 are used as the dc-voltage sources V_{dc1} and V_{dc2}.
2) The reference value of the dc-capacitor voltage is set as $V_C^* = 75$ V.
3) An air-core inductor with linear frequency characteristics is used. Consequently, the actual inductance values are $L_{\text{CBC}} = 0.4$ mH for the CBC and $L_{\text{BCSAC-PS}} = 0.334$ mH for the BCSAC-PS.
4) The reference value of the inductor current, i_L^*, can be either positive or negative, where positive current implies that the power flows from V_{dc1} to V_{dc2}, while negative current implies the opposite.
5) A combination of Texas Instruments TMS320C6678 DSP and Altera Cyclone IV E EP4CE30F29C7 FPGA is used to control the model. Specifically, the FPGA is used to generate the triangular carriers, to compare the triangular carriers with the duty ratios (i.e., d_M, d_{A1}, and d_{A2}) calculated by the DSP, and to generate the PWM signals.
6) The Tektronix oscilloscope DPO4104B-L with a frequency band of 1 GHz is used to record the experimental waveforms. The current waveform (i.e., i_L) is measured using the Tektronix current probe TCP0020 with a frequency band of 50 MHz, while the voltage waveforms (i.e., v_M, v_A, v_L, and v_C) are measured using the Tektronix high-voltage differential probes THDP0200 with a frequency band of 200 MHz.

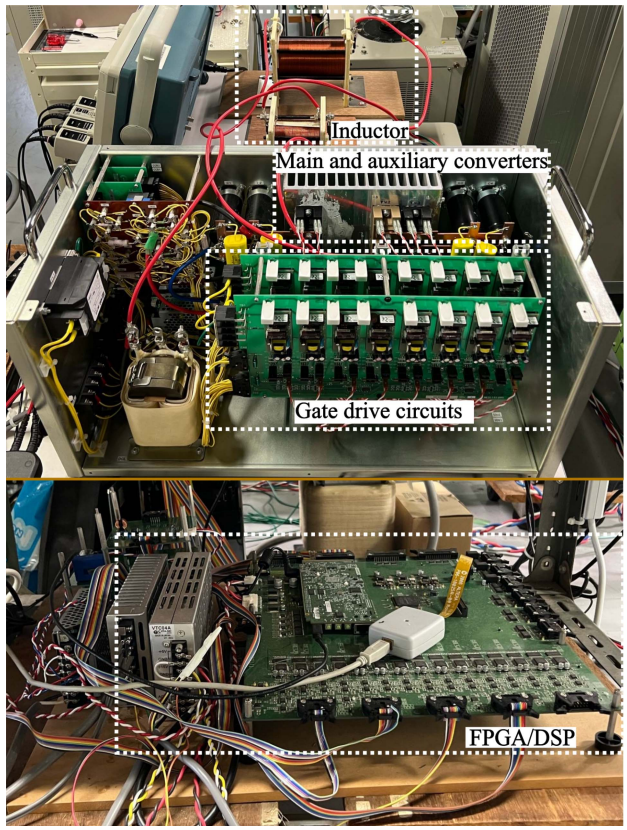

Fig. 14. Experimental setup using down-scaled model.

TABLE III
Parameters of the Experiments

P	Rated power	2 kW
V_{dc1}	DC-voltage source 1	150 V
L_{CBC}	Inductance of the CBC	0.4 mH
$L_{\text{BCSAC-PS}}$	Inductance of the BCSAC-PS	0.334 mH
C	Capacitance of the dc-capacitor	0.4 mF
V_C^*	DC-capacitor voltage	75 V
f_{SM}	Switching frequency (main converter)	5 kHz
f_{SA}	Switching frequency (auxiliary converter)	5 kHz

The following experiments are conducted under both the dc and ac component-based controls, where the experimental parameters are listed in Table III.

DC component-based control

1) Experiment to measure ripple current values of the BCSAC-PS and CBC under $V_{\text{dc1}} = 150$ V and $i_L^* = -10$ A, where v_C is initially charged to 75 V.
2) Experiment to observe the operation of BCSAC-PS during the steady-state under $V_{\text{dc1}} = 150$ V, $V_{\text{dc2}} = 65$ V, and $i_L^* = -10$ A, where v_C is initially charged to 75 V.
3) Experiment to observe the transient behavior of the BCSAC-PS during the initial charging of v_C from 0 to 75 V, where $i_L^* = -20$ A.

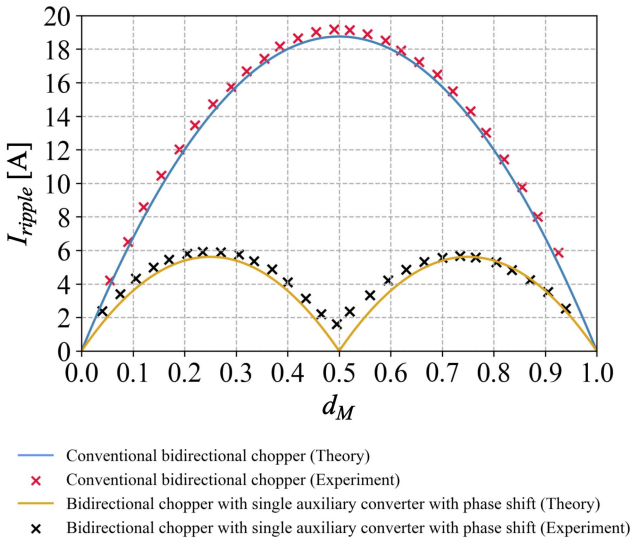

Fig. 15. Theoretical and experimental ripple currents of CBC and BCSAC-PS under $V_{\rm dc1} = 150$ V and $i_L^* = -10$ A.

4) Experiment to observe the transient behavior of the BCSAC-PS during step change of $V_{\rm dc1}$ from 150 to 140 V, where $i_L^* = -20$ A.

AC component-based control

1) Experiment to observe the operation of BCSAC-PS during the steady-state under $V_{\rm dc1} = 150$ V, $V_{\rm dc2} = 75$ V, and $i_L^* = 0$ A, where v_C is initially charged to 75 V.
2) Experiment to observe the transient behavior of the BCSAC-PS during the initial charging of v_C from 0 to 75 V, where $i_L^* = 0$ A.
3) Experiment to observe the transient behavior of the BCSAC-PS during the ramp change of v_C from 75 to 85 V and then 85 to 75 V, where $i_L^* = 0$ A.

Coordinated control

1) Experiment to observe the coordinated operation of the ac and dc component-based controls during the ramp change of i_L from 0 A to -10 A and then -10 A to 0 A.

It should be noted that the down-scaled model used to conduct the experiments comes with several limitations that could affect the produced power loss. Thus, experiments to verify power loss and efficiency of the BCSAC-PS are not done in this article, and should be deferred for future research.

B. Switching-Ripple Current

The results of the switching-ripple current for the BCSAC-PS and CBC, based on the theoretical analysis and the experiments done under negative current using dc component-based control, are given in Fig. 15. For the CBC, the theoretical result is shown in blue line and the experimental results are shown in the red crosses, while those for BCSAC-PS are shown in gold line and black crosses, respectively. The experiments are done by setting $V_{\rm dc1} = 150$ V and $i_L^* = -10$ A, while v_C is initially charged to 75 V. Meanwhile, d_M is progressively changed by setting $V_{\rm dc2}$ from 10 to 140 V. Here, the negative current signifies that it flows from the low-voltage side to the high-voltage side.

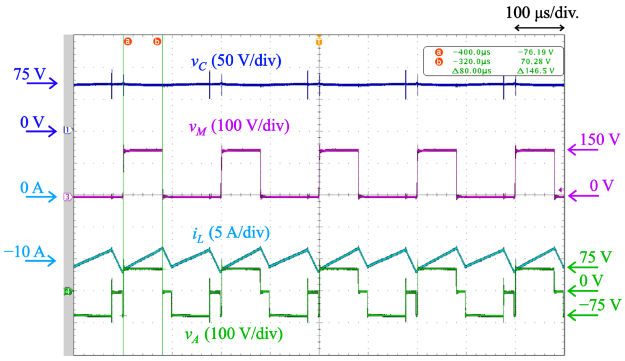

Fig. 16. Experimental steady-state waveforms of BCSAC-PS using DC component-based control for $V_{\rm dc1} = 150$ V, $V_{\rm dc2} = 65$ V, and $i_L^* = -10$ A.

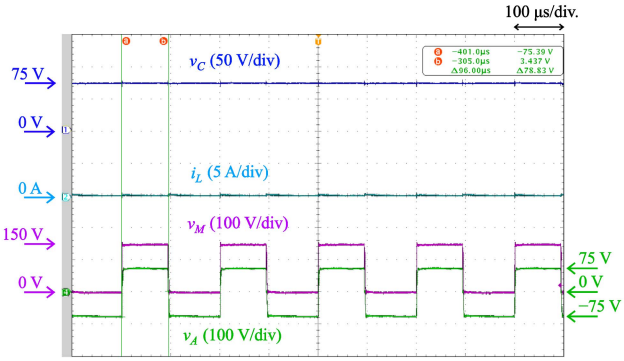

Fig. 17. Experimental steady-state waveforms of BCSAC-PS using AC component-based control for $V_{\rm dc1} = 150$ V, $V_{\rm dc2} = 75$ V, and $i_L^* = 0$ A.

Fig. 15 shows that there is a consistency between the theoretical and experimental results on all choppers, albeit the small difference seen in the BCSAC-PS. This difference is because the voltage reference v_B^* is assumed to be nonexistent in the theoretical analysis, which is not the case in the experiments, and it has some effects on the $I_{\rm ripple}$ calculation. However, the difference is insignificant compared to the current value, and it will become smaller in the actual system with higher operating voltage and current.

It is also shown that the CBC has a maximum ripple current of 19.2 A, which is obtained when $d_M = 0.49$. Meanwhile, the BCSAC-PS has a maximum ripple current of around 5.4 A, which is obtained when $d_M = 0.24$ and 0.74.

C. Steady-State Operation

The steady-state experimental waveforms of the BCSAC-PS under $V_{\rm dc1} = 150$ V, $V_{\rm dc2} = 65$ V, and $i_L^* = -10$ A using dc component-based control are given in Fig. 16, where negative current signifies that the current flows from the low-voltage side to the high-voltage side, while the steady-state experimental waveforms of the BCSAC-PS under $V_{\rm dc1} = 150$ V, $V_{\rm dc2} = 75$ V, and $i_L^* = 0$ A using ac component-based control are given in Fig. 17. In both Figs. 16 and 17, the main converter voltage v_M is a rectangular wave with both dc and ac components, where its value changes between 150 V ($=V_{\rm dc1}$) and 0 V, while

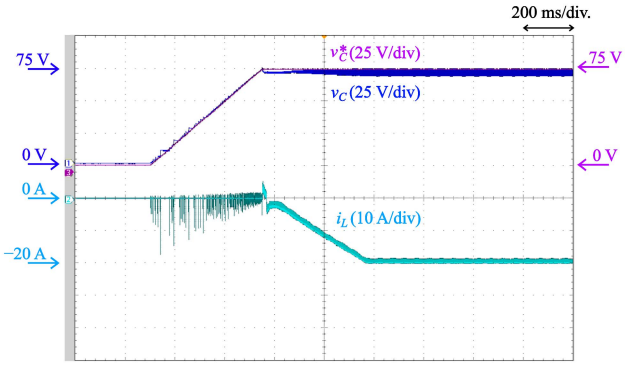

Fig. 18. Experimental waveforms of BCSAC-PS using DC component-based control for $V_{dc1} = 150$ V and $V_{dc2} = 85$ V during the initial charging procedure.

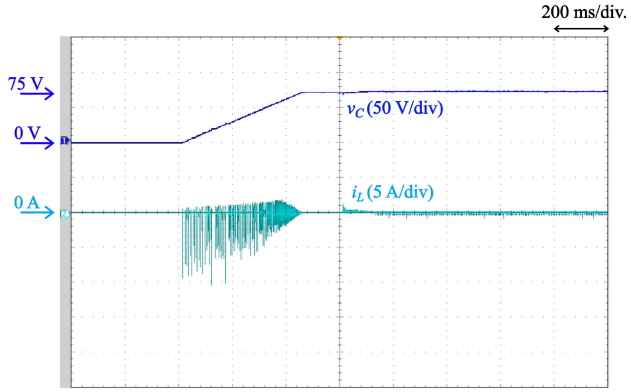

Fig. 19. Experimental waveforms of BCSAC-PS using AC component-based control for $V_{dc1} = 150$ V and $V_{dc2} = 75$ V during the initial charging procedure.

the auxiliary converter voltage v_A is a rectangular wave that alternates between -75 V ($=-V_C$), 0 V, and 75 V ($=V_C$). Based on the displayed ON-period in Fig. 16, the actual value of the duty ratio is $d_M = 0.4$, which is lower than the theoretical value of 0.43 obtained from (17). This is due to the existence of the voltage reference v_B^* in the main converter control, as given in Fig. 3. Similarly, the actual value of the duty ratio in Fig. 17 is $d_M = 0.48$, which is lower than the theoretical value of 0.5 obtained from (17). This is due to the existence of the voltage command v_i^* in the main converter control, as given in Fig. 5.

From Fig. 16, it can be seen that the controls of the dc-capacitor voltage, v_C, and the dc inductor current, $(i_L)_{avg}$, are achieved without steady-state error. v_C can be regulated to 75 V ($=0.5V_{dc1}$), while $(i_L)_{avg}$ can be regulated to -10 A with a ripple current of 4.1 A. Meanwhile, the theoretical value of the ripple current obtained from (14) is around 3.59 A. Thus, there is consistency between the experimental and theoretical values of the ripple current, where the slight difference is due to the existence of v_B^* in the main converter control that affects the value of d_M. Fig. 17 shows that the dc-capacitor voltage and dc inductor current controls are achieved without steady-state error when $i_L^* = 0$ A, where v_C similarly can be regulated to 75 V and $(i_L)_{avg}$ can be regulated to 0 A.

D. Transient-State Operation

The transient experimental waveforms of the BCSAC-PS during the initial charging procedure using the dc component and ac component-based controls are given in Figs. 18 and 19, respectively. Since V_{dc1} is set as the high-voltage side ($V_{dc1} = 150$ V) and V_{dc2} is the low-voltage side, where $V_{dc2} = 85$ V in Fig. 18 and $V_{dc2} = 75$ V in Fig. 19, V_{dc1} is used to charge the capacitor. To send the power from V_{dc1} to the capacitor, the full-bridge auxiliary converter initially operates in charging mode (i.e., S_3 and S_6 are ON, while S_4 and S_5 are OFF). In the main converter, S_2 is always OFF, while S_1 is controlled to change its duty ratio, d_M, based on the traditional PI control, which is then used for the feedback control of the v_C (under dc component-based control) and i_L (under ac component-based control). From Fig. 18, v_C is charged to 75 V in 400 ms, where the BCSAC-PS then gets into normal operation, and i_L drops into its reference value at -20 A in approximately 400 ms. Meanwhile, v_C in Fig. 19 is charged to 75 V in around 450 ms, and the control of i_L at 0 A is achieved. Overall, the initial charging procedure using the dc component and ac component-based controls can be completed without any overvoltage or overcurrent problem.

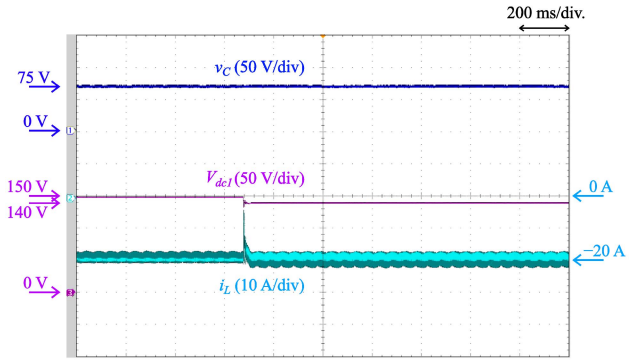

Fig. 20. Experimental waveforms of BCSAC-PS using DC component-based control for $V_{dc2} = 10$ V and $i_L^* = -20$ A, where there is a step change in V_{dc1} from 150 to 140 V.

The transient experimental waveforms of the BCSAC-PS during a step change of V_{dc1} using the dc component-based control done under $V_{dc2} = 10$ V and $i_L^* = -20$ A are given are Fig. 20. It shows that V_{dc1} can be successfully reduced from 150 to 140 V in approximately 40 ms with no undervoltage. However, a slight jump can be observed in the inductor current when the step change is started, that is caused by the effect of the reduction in V_{dc1} on v_L. Furthermore, it produces higher d_M, which ultimately results in higher ripple current when the value of V_{dc2} is considered. Meanwhile, dc-capacitor voltage, v_C, can be stably regulated with no error during the transient state.

The transient experimental waveforms of the BCSAC-PS during a ramp change of v_C using the ac component-based control under $V_{dc1} = 150$ V, $V_{dc2} = 75$ V, and $i_L^* = 0$ V are given in Fig. 21. It shows that v_C is able to rise from 75 to 85 V, and drop from 85 to 75 V, with no overvoltage and undervoltage, meaning that the dc-capacitor voltage control based on the ac component-based control is valid. Furthermore, the inductor

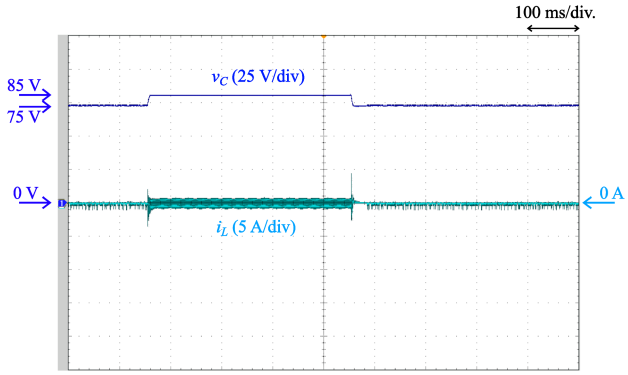

Fig. 21. Experimental waveforms of BCSAC-PS using AC component-based control for $V_{\rm dc1} = 150$ V, $V_{\rm dc2} = 75$ V, and $i_L^* = 0$ A, where there is a ramp change in v_C from 75 to 85 V and then from 85 to 75 V.

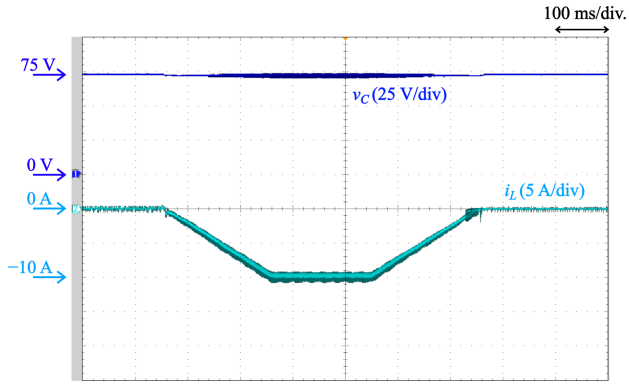

Fig. 22. Experimental waveforms of coordinated operation between the AC and DC component-based controls for $V_{\rm dc1} = 150$ V and $V_{\rm dc2} = 75$ V, where there is a ramp change in i_L from 0 to -10 A and then from -10 to 0 A.

current can be stably controlled, with the observed increase in ripple current. This is caused by the effect of the change in v_C on v_L.

E. Coordinated Operation

The transient experimental waveforms of the BCSAC-PS during a ramp change of i_L under $V_{\rm dc1} = 150$ V and $V_{\rm dc2} = 75$ V using a coordination of both ac and dc component-based controls are shown in Fig. 22, where the ac component-based control is applied when $i_L = 0$ A and the dc component-based control is applied when $i_L \neq 0$ A. It shows that i_L is able to decrease from 0 A to -10 A in 200 ms, and increase from -10 to 0 A in 200 ms, with no overcurrent and undercurrent. Furthermore, the dc-capacitor voltage can be stably regulated using the ac component-based control when $i_L = 0$ A and dc component-based control when $i_L = -10$ A. This shows that the two control methods can operated in coordination.

VI. Conclusion

This article has proposed the supplementary application of ac component-based control and the application of phase shift to a bidirectional chopper with a single auxiliary full-bridge converter (BCSAC) that operates under the following conditions: 1) Both the main and auxiliary converters have the same switching frequencies ($f_{\rm SM} = f_{\rm SA}$), and 2) The dc-capacitor voltage is half of the high-voltage-side dc-source voltage ($V_C = V_{\rm dc1}/2$). Theoretical analysis show that the BCSAC-PS is able to reduce the switching-ripple current to $1/4$ of that produced by the CBC, which is more significant compared to the $4/9$ reduction achieved by the BCSAC-NPS. Consequently, the BCSAC-PS enables smaller inductor volume comparable to the TLFC-PS, that is 62.3% and 38.8% less than those of the CBC and BCSAC-NPS, respectively. Meanwhile, loss analysis shows that the BCSAC-PS produces lower losses than the BCSAC-NPS. Even though the efficiency is slightly lower than the CBC and TLFC-PS, the BCSAC-PS can achieve high efficiency performance that is better than the BCSAC-NPS. Finally, experimental results using a 2 kW down-scaled model have shown consistency with the theoretical results of the switching-ripple current, and verify the operations and controls of the BCSAC-PS during the steady and transient states, along with the coordinated operation of the ac and dc component-based controls, where the former is used when the dc inductor current is zero and the latter is used when the dc inductor current is not zero.

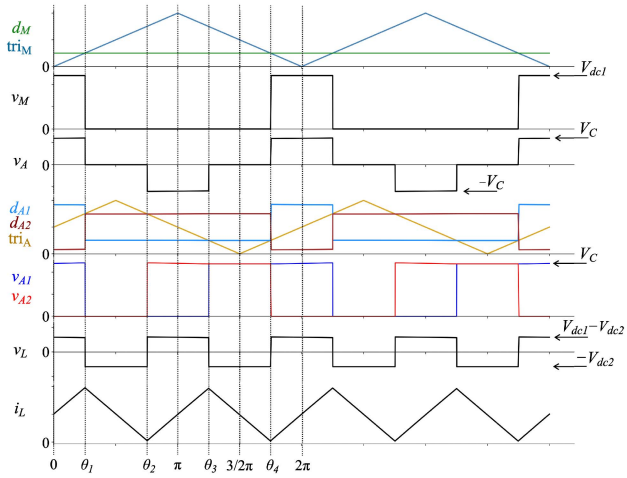

Fig. 23. Ideal voltage and current waveforms of the BCSAC-PS when $d_M = 0.25$.

Appendix

The following theoretical analysis of the switching-ripple current focuses on $0 \leq d_M < 0.5$. Based on the ideal waveforms when $d_M = 0.25$ given in Fig. 23, d_M intersects $\rm tri_M$ at θ_1 and θ_4, while d_{A1} and d_{A2} intersect $\rm tri_A$ at θ_3 and θ_2, respectively. Furthermore, the relationships $\theta_2 \geq \theta_1$ and $\theta_4 \geq \theta_3$ are assumed. In the figure, θ_1 and θ_4 are given by

$$\theta_1 = \pi d_M \tag{23}$$

$$\theta_4 = 2\pi - \pi d_M. \tag{24}$$

Based on (1), v_M is given by

$$v_M = \begin{cases} V_{\rm dc1} & (0 \leq \theta < \theta_1, \theta_4 < \theta \leq 2\pi) \\ 0 & (\theta_1 \leq \theta \leq \theta_4). \end{cases} \tag{25}$$

Under the given value of d_M, d_{A1} and d_{A2} can be determined based on (6) by

$$d_{A1} = \begin{cases} -\frac{v_i^*}{V_{\rm dc1}} + 1 & (0 \le \theta < \theta_1, \theta_4 < \theta \le 2\pi) \\ -\frac{v_i^*}{V_{\rm dc1}} + \frac{0.5}{d_M - 1} & \\ +1 & (\theta_1 \le \theta \le \theta_4) \end{cases} \tag{26}$$

$$d_{A2} = \begin{cases} \frac{v_i^*}{V_{\rm dc1}} & (0 \le \theta < \theta_1, \theta_4 < \theta \le 2\pi) \\ \frac{v_i^*}{V_{\rm dc1}} - \frac{0.5}{d_M - 1} & (\theta_1 \le \theta \le \theta_4) \end{cases} \tag{27}$$

where their values range between $0 \le d_{A1} \le 1$ and $0 \le d_{A2} \le 1$.

From Fig. 23, (26), and (27), θ_2 and θ_3 can be determined by

$$\theta_2 = \pi \left(-\frac{v_i^*}{V_{\rm dc1}} + \frac{0.5}{d_M - 1} + \frac{3}{2} \right) \tag{28}$$

$$\theta_3 = \pi \left(\frac{v_i^*}{V_{\rm dc1}} - \frac{0.5}{d_M - 1} + \frac{1}{2} \right). \tag{29}$$

Furthermore, the value of v_A can be expressed as

$$v_A = \begin{cases} V_C & (0 \le \theta \le \theta_1) \\ 0 & (\theta_1 < \theta \le \theta_2) \\ -V_C & (\theta_2 < \theta \le \theta_3) \\ 0 & (\theta_3 < \theta \le \theta_4) \\ V_C & (\theta_4 < \theta \le 2\pi). \end{cases} \tag{30}$$

In the BCSAC-PS, the power flowing into the auxiliary converter, $P_{\rm aux}$, is equivalent to $P_{\rm aux} = v_A i_L$. When i_L is a dc quantity, the voltage command v_i^* in the main converter control will be regulated to ensure that only ac component exists in v_A under the steady state (see Section III), which makes its average value in one switching-period to be zero. Consequently, based on (23), (24), (28), and (29), the voltage command v_i^* can be expressed as

$$v_i^* = V_{\rm dc1} \frac{d_M(2d_M - 1)}{2(d_M - 1)}. \tag{31}$$

Substituting (31) into (28) and (29) gives

$$\theta_2 = \pi(-d_M + 1) \tag{32}$$

$$\theta_3 = \pi(d_M + 1). \tag{33}$$

Based on (23), (24), (32), and (33), the relationships $\theta_1 \le \theta_2$ and $\theta_3 \le \theta_4$ always hold in the range $0 \le d_M < 0.5$, which validates the prior assumptions.

Next, the validity of the assumptions that θ_2 and θ_3 are the intersection points between tri_A with d_{A2} and d_{A1} will be verified. Substituting (31) into (26) and (27) gives

$$d_{A1} = \begin{cases} -d_M & \\ -\frac{1}{2(d_M - 1)} + \frac{1}{2} & (0 \le \theta < \theta_1, \theta_4 < \theta \le 2\pi) \\ -d_M + \frac{1}{2} & (\theta_1 \le \theta \le \theta_4) \end{cases} \tag{34}$$

$$d_{A2} = \begin{cases} d_M + \frac{1}{2(d_M - 1)} & \\ +\frac{1}{2} & (0 \le \theta < \theta_1, \theta_4 < \theta \le 2\pi) \\ d_M + \frac{1}{2} & (\theta_1 \le \theta \le \theta_4). \end{cases} \tag{35}$$

Based on Fig. 23, the values tri_M at θ_1 and θ_4 correspond to d_M. Meanwhile, the value of d_{A2} at θ_1 is obtained from (35) as $d_M + \frac{1}{2}$, which always gives higher value than d_M in the range of $0 \le d_M < 0.5$. This signifies that the phase θ_2 that satisfies $\theta_2 \ge \theta_1$ always exists for d_M in the range of $0 \le d_M < 0.5$. Meanwhile, the value of d_{A1} at θ_4 is obtained from (34) as $-d_M + \frac{1}{2}$, which only gives higher value than d_M in the range of $0 \le d_M < 0.25$. However, when the phase shift applied to tri_A is considered, the phase θ_3 that satisfies $\theta_3 \le \theta_4$ similarly always exists for d_M in the range of $0 \le d_M < 0.5$.

Finally, the inductor voltage can be obtained by KVL, while considering (25) and (30), as

$$\begin{aligned} v_L &= v_M - v_A - V_{\rm dc2} \\ &= \begin{cases} 0.5V_{\rm dc1} - V_{\rm dc2} & (0 \le \theta \le \theta_1) \\ -V_{\rm dc2} & (\theta_1 < \theta \le \theta_2) \\ 0.5V_{\rm dc1} - V_{\rm dc2} & (\theta_2 < \theta \le \theta_3) \\ -V_{\rm dc2} & (\theta_3 < \theta \le \theta_4) \\ 0.5V_{\rm dc1} - V_{\rm dc2} & (\theta_4 < \theta \le 2\pi) \end{cases} \end{aligned} \tag{36}$$

where the relationship $V_C = \frac{V_{\rm dc1}}{2}$ is used. Since $d_M = \frac{V_{\rm dc2}}{V_{\rm dc1}} < 0.5$, the followings occur:

1) i_L increases in the period of $0 \le \theta \le \theta_1$ $(= I_{\rm up1})$, $\theta_2 < \theta \le \theta_3$ $(= I_{\rm up2})$, and $\theta_4 < \theta \le 2\pi$ $(= I_{\rm up3})$;
2) i_L decreases in the period of $\theta_1 < \theta \le \theta_2$ $(= I_{\rm down1})$ and $\theta_3 < \theta \le \theta_4$ $(= I_{\rm down2})$;

where the increasing and decreasing rates are consistent under the steady state. From (23) and (36), $I_{\rm up1}$ is given by

$$\begin{aligned} I_{\rm up1} &= \frac{1}{\omega L} \int_0^{\theta_1} (0.5V_{\rm dc1} - V_{\rm dc2})\, d\theta \\ &= \frac{V_{\rm dc1}}{2f_{\rm SM}L} \frac{(1 - 2d_M)d_M}{2}. \end{aligned} \tag{37}$$

From (23), (32), and (36), $I_{\rm down1}$ is given by

$$\begin{aligned} I_{\rm down1} &= -\frac{1}{\omega L} \int_{\theta_1}^{\theta_2} -V_{\rm dc2}\, d\theta \\ &= \frac{V_{\rm dc1}}{2f_{\rm SM}L}(1 - 2d_M)(d_M). \end{aligned} \tag{38}$$

From (22), (33), and (36), $I_{\rm up2}$ is given by

$$\begin{aligned} I_{\rm up2} &= \frac{1}{\omega L} \int_{\theta_2}^{\theta_3} (0.5V_{\rm dc1} - V_{\rm dc2})\, d\theta \\ &= \frac{V_{\rm dc1}}{2f_{\rm SM}L}(1 - 2d_M)d_M. \end{aligned} \tag{39}$$

From (24), (33), and (36), $I_{\rm down2}$ is given by

$$\begin{aligned} I_{\rm down2} &= -\frac{1}{\omega L} \int_{\theta_3}^{\theta_4} -V_{\rm dc2}\, d\theta \\ &= \frac{V_{\rm dc1}}{2f_{\rm SM}L}(1 - 2d_M)d_M. \end{aligned} \tag{40}$$

From (24) and (36), $I_{\rm up3}$ is given by

$$\begin{aligned} I_{\rm up3} &= \frac{1}{\omega L} \int_{\theta_4}^{2\pi} (0.5V_{\rm dc1} - V_{\rm dc2})\, d\theta \\ &= \frac{V_{\rm dc1}}{2f_{\rm SM}L} \frac{(1 - 2d_M)d_M}{2}. \end{aligned} \tag{41}$$

From (37)–(41), the relationship $I_{\text{down1}} = I_{\text{up2}} = I_{\text{down2}} > I_{\text{up1}} = I_{\text{up3}}$ always holds in the range $0 \leq d_M < 0.5$. Thus, the peak-to-peak ripple current, I_{ripple}, when $0 \leq d_M < 0.5$ is given by

$$I_{\text{ripple}} = \frac{V_{\text{dc1}}}{2 f_{\text{SM}} L}(1 - 2d_M)d_M. \tag{42}$$

Similarly, the theoretical analysis when $0.5 \leq d_M \leq 1$ can be done based on the ideal waveforms when d_M is within the range.

REFERENCES

[1] D. Ramsey, T. Letrouve, A. Bouscayrol, and P. Delarue, "Comparison of energy recovery solutions on a suburban DC railway system," *IEEE Trans. Transp. Electrific.*, vol. 7, no. 3, pp. 1849–1857, Sep. 2021.

[2] M. Saeed et al., "Onboard energy storage systems for railway: Present and trends," *IEEE Open J. Ind. Appl.*, vol. 4, pp. 238–259, 2023.

[3] M. Lyu, D. Kong, and M. Miyatake, "Optimal energy dispatch of energy storage system as a shared infrastructure between dc railway network and DC micro grid," in *Proc. 25th Int. Conf. Elect. Mach. Syst.*, 2022, pp. 1–6.

[4] C. Wu, S. Lu, F. Xue, L. Jiang, and M. Chen, "Optimal sizing of onboard energy storage devices for electrified railway systems," *IEEE Trans. Transp. Electrific.*, vol. 6, no. 3, pp. 1301–1311, Sep. 2020.

[5] B. V. Kumar, R. K. Singh, and R. Mahanty, "A modified non-isolated bidirectional DC-DC converter for EV/HEV's traction drive systems," in *Proc. IEEE Int. Conf. Power Electron., Drives Energy Syst.*, 2016, pp. 1–6.

[6] S. P. Sunddararaj, S. S. Rangarajan, U. Subramaniam, E. R. Collins, and T. Senjyu, "A new topology of DC-DC converter with bidirectional power flow capability coupled with a nine multilevel inverter for EV applications," in *Proc. 7th Int. Conf. Elect. Energy Syst.*, 2021, pp. 177–182.

[7] Y. Jia et al., "Unified discrete-time modeling and digital control of bidirectional chopper converter," in *Proc. 11th Int. Conf. Power, Energy Elect. Eng.*, 2021, pp. 64–70.

[8] O. Hegazy, J. V. Mierlo, and P. Lataire, "Analysis, modeling, and implementation of a multidevice interleaved DC/DC converter for fuel cell hybrid electric vehicles," *IEEE Trans. Power Electron.*, vol. 27, no. 11, pp. 4445–4458, Nov. 2012.

[9] K. Takao et al., "High-power converters with high switching frequency operation using SiC-PiN diodes and Si-IEGTs," in *Proc. 1st Int. Conf. Electric Power Equip. - Switching Technol.*, 2011, pp. 412–417.

[10] N. Soltau, E. Wiesner, E. Stumpf, S. Idaka, and K. Hatori, "Electric-energy savings using 3.3 kV full-SiC power-modules in traction applications," in *Proc. 15th Int. Conf. Ecological Veh. Renewable Energies*, 2020, pp. 1–5.

[11] K. Yasui et al., "A 3.3 kV 1000 a high power density SiC power module with sintered copper die attach technology," in *Proc. Int. Exhib. Conf. Power Electron., Intell. Motion, Renewable Energy Energy Manage.*, 2019, pp. 1–6.

[12] W. Qi, S. Li, H. Yuan, S.-C. Tan, and S.-Y. Hui, "High-power-density single-phase three-level flying-capacitor buck PFC rectifier," *IEEE Trans. Power Electron.*, vol. 34, no. 11, pp. 10833–10844, Nov. 2019.

[13] S. d. S. Carvalho, M. Halamíček, N. Vukadinović, and A. Prodić, "Digital PWM for multi-level flying capacitor converters with improved output resolution and flying capacitor voltage controller stability," in *Proc. IEEE 19th Workshop Control Model. Power Electron.*, 2018, pp. 1–7.

[14] Q. Nguyen, Q.-T. Nguyen, H.-D. Han, L. Pham-Nguyen, and H.-P. Le, "Integrated modified three-level buck converter with flying capacitor-voltage self-balance," in *Proc. IEEE 9th Int. Conf. Commun. Electron.*, 2022, pp. 450–454.

[15] Z. Ye, Y. Lei, Z. Liao, and R. C. N. Pilawa-Podgurski, "Investigation of capacitor voltage balancing in practical implementations of flying capacitor multilevel converters," *IEEE Trans. Power Electron.*, vol. 37, no. 3, pp. 2921–2935, Mar. 2022.

[16] J. Kim et al., "A proposed fast charging and high-power system for wireless railway trains adopting the input voltage sharing topology and the balancing control scheme," *IEEE Trans. Ind. Electron.*, vol. 67, no. 8, pp. 6407–6417, Aug. 2020.

[17] J. Fabre, P. Ladoux, E. Solano, G. Gateau, and J.-M. Blaquière, "MVDC three-wire supply systems for electric railways: Design and test of a full SiC multilevel chopper," *IEEE Trans. Ind. Appl.*, vol. 53, no. 6, pp. 5820–5830, Nov./Dec. 2017.

[18] Z. Chen, S. Liu, Y. Chen, X. Fan, and Y. Ma, "A current-injection-based flying capacitor balancing circuit for three-level DC-DC converter," in *Proc. IEEE Int. Symp. Circuits Syst.*, 2022, pp. 2630–2634.

[19] W. Ma, B. Zhang, and D. Qiu, "Robust single-loop control strategy for four-level flying-capacitor converter based on switched system theory," *IEEE Trans. Ind. Electron.*, vol. 70, no. 8, pp. 7832–7844, Aug. 2023.

[20] D. H. Zhou, J. Celikovic, Y. Elasser, D. Maksimovic, and M. Chen, "Balancing limits of flying capacitor voltages in coupled inductor fcml converters," in *Proc. IEEE 23rd Workshop Control Model. Power Electron.*, 2022, pp. 1–8.

[21] H. Ohnishi and M. Hagiwara, "Experimental verification of a bidirectional chopper for battery energy storage systems capable of reduction in size and weight of an inductor," in *Proc. IEEE Energy Convers. Congr. Expo.*, 2017, pp. 197–204.

[22] H. J. Ahmad, H. Ohnishi, and M. Hagiwara, "Start-up and transient operation of a bidirectional chopper with an auxiliary converter," in *Proc. Int. Power Electron. Conf. (IPEC-Niigata 2018 -ECCE Asia)*, 2018, pp. 3273–3279.

[23] M. Hagiwara and H. J. Ahmad, "High switching frequency operation of bidirectional chopper with auxiliary converter for DC electric railways," in *Proc. IEEE Int. Future Energy Electron. Conf.*, 2021, pp. 1–6.

[24] H. J. Ahmad and M. Hagiwara, "A compact high-power noninverting bidirectional buck–boost chopper for onboard battery energy storage systems," *IEEE Trans. Power Electron.*, vol. 37, no. 2, pp. 1722–1735, Feb. 2022.

[25] H. J. Ahmad and M. Hagiwara, "Interleaved bidirectional chopper with auxiliary converters for battery energy storage systems," in *Proc. IEEE Appl. Power Electron. Conf. Expo.*, 2020, pp. 2090–2097.

[26] H. J. Ahmad and M. Hagiwara, "Interleaved bidirectional chopper with auxiliary converters for DC electric railways," *IEEE Trans. Power Electron.*, vol. 36, no. 5, pp. 5336–5347, May 2021.

[27] H. J. Ahmad and M. Hagiwara, "Modified phase-shifted PWM for interleaved bidirectional chopper with auxiliary converters," in *Proc. IEEE 12th Energy Convers. Congr. Expo. - Asia*, 2021, pp. 755–761.

[28] G. A. M. Nasution, M. Matsumoto, and M. Hagiwara, "Switching-ripple current evaluation of bidirectional chopper with single auxiliary full-bridge converter," in *Proc. IEEE Energy Convers. Congr. Expo.*, 2023, pp. 6357–6364.

[29] G. A. M. Nasution, M. Matsumoto, and M. Hagiwara, "Bidirectional chopper with single-cell auxiliary full-bridge converter for onboard battery energy storage system," *IEEE Trans. Power Electron.*, vol. 39, no. 8, pp. 10021–10033, Aug. 2024.

[30] R. Barrera-Cardenas, T. Isobe, and M. Molinas, "Optimal design of air-core inductor for medium/high power dc-dc converters," in *Proc. IEEE 17th Workshop Control Model. Power Electron.*, 2016, pp. 1–8.

[31] S. R. Meher, D. Gautam, and R. Singh, "Wireless power transfer using EF_2 inverter with fixed coil capacitor and air core inductor," in *Proc. IEEE Appl. Power Electron. Conf. Expo.*, 2020, pp. 3588–3593.

[32] C. Shetty et al., "Analytical expressions for inductances of 3-D air-core inductors for integrated power supply," *IEEE Trans. Emerg. Sel. Topics Power Electron.*, vol. 10, no. 2, pp. 1363–1383, Apr. 2022.

[33] G. Abad, *Power Electronics and Electric Drives for Traction Applications*. Hoboken, NJ, USA: Wiley, 2016. [Online]. Available: https://books.google.co.jp/books?id=_loanQAACAAJ

[34] 2024. [Online]. Available: https://www.electronicon.com/fileadmin/inhalte/PDF-Dateien/Kataloge_und_Broschueren/200.003-020030_PK16.pdf

[35] 2013. [Online]. Available: https://felib.fujielectric.co.jp/download/b9ca89b2-8198-4480-9ebd-b8f5dd0a17ed/?lang=ja

[36] 2020. [Online]. Available: https://www.mitsubishielectric.com/semiconductors/content/product/powermodule/igbt/t_series/cm1000dx-24t_e.pdf

[37] J. Fabre et al., "Characterization and implementation of resonant isolated DC/DC converters for future MVdc railway electrification systems," *IEEE Trans. Transp. Electrific.*, vol. 7, no. 2, pp. 854–869, Jun. 2021.

[38] M. Alam, K. Kumar, and V. Dutta, "Comparative efficiency analysis for silicon, silicon carbide MOSFETs and IGBT device for DC–DC boost converter," *SN Appl. Sci.*, vol. 1, 2019, Art. no. 1700.

[39] A. Kahwa, H. Obara, and Y. Fujimoto, "Estimation and analysis of power loss in a reduced switches count H-bridge multilevel inverter," in *Proc. IEEE Int. Conf. Mechatron.*, vol. 1, 2019, pp. 25–30.

[40] J. Qi et al., "Temperature dependence of dynamic performance characterization of 1.2-kV SiC power mosfets compared with Si IGBTs for wide temperature applications," *IEEE Trans. Power Electron.*, vol. 34, no. 9, pp. 9105–9117, Sep. 2019.

[41] T. Ibuchi and T. Funaki, "Validation of the air-core inductor copper loss model for high-frequency power conversion applications," in *Proc. Int. Symp. Electromagn. Compat.*, 2013, pp. 561–566.

Ghiffari Aby Malik Nasution (Graduate Student Member, IEEE) was born in Bekasi, Indonesia, in 1997. He received the B.Eng. degree in transdisciplinary science and engineering and the M.Eng. degree in energy science and engineering from the Tokyo Institute of Technology, Tokyo, Japan, in 2020 and 2022, respectively. He is currently working toward the Ph.D. degree in energy science and engineering with the Department of Electrical and Electronic Engineering, Institute of Science Tokyo (formerly Tokyo Institute of Technology), Tokyo.

His research interests include dc–dc converters for hybrid renewable energy system and electric trains/vehicles.

Makoto Hagiwara (Senior Member, IEEE) was born in Tokyo, Japan, in 1979. He received the B.S., M.S., and Ph.D. degrees in electrical engineering from the Tokyo Institute of Technology, Tokyo, Japan, in 2001, 2003, and 2006, respectively.

From 2006 to 2015, he was an Assistant Professor with the Department of Electrical and Electronic Engineering, Tokyo Institute of Technology. Since 2015, he has been an Associate Professor in the same institute, whose name is changed to Institute of Science Tokyo from 2024. His research interests include dc-to-dc converters for electric trains/vehicles, high-voltage high-power converters for utility applications and renewable energies, and HVdc technologies.

Dr. Hagiwara was the recipient of the 2010 International Power Electronics Conference (IPEC-Sapporo/ECCE-Asia) second prize paper award, the 2012 and 2013 IEEE Industry Applications Society Industrial Power Converter Committee first prize paper awards, the 2014 Isao Takahashi Power Electronics Award, the 2023 TPEL AE Excellence Award, and the 2024 Nagamori Award.